Structural origin of perpendicular magnetic anisotropy in epitaxial $CoPt_3$ nanostructures grown on $WSe_2(0001)$

F. Liscio,[1,2] M. Maret,[1] C. Meneghini,[2,3] S. Mobilio,[2,3,4] O. Proux,[5] D. Makarov,[6] and M. Albrecht[6]
[1]*SIMAP, INP Grenoble-CNRS-UJF, 1130 rue de la Piscine, BP 75, F-38402 Saint Martin d'Hères, France*
[2]*Dipartimento di Fisica "E. Amaldi," Università di Roma Tre, via della Vasca Navale 84, I-00146 Roma, Italy*
[3]*CNR-TASC, c/o GILDA at ESRF, Grenoble, France*
[4]*Laboratori Nazionali di Frascati, INFN, via E. Fermi 40, I-00044 Frascati, Italy*
[5]*Observatoire des Sciences de l'Univers de Grenoble, 414 rue de la Piscine, F-38400 Saint Martin d'Hères, France*
[6]*Institute of Physics, Chemnitz University of Technology, D-09107 Chemnitz, Germany*
(Received 28 September 2009; published 16 March 2010)

We present a detailed analysis of the local ordering in $CoPt_3$ nanostructures epitaxially grown on $WSe_2(0001)$ and NaCl(001) low-energy surfaces. Polarized extended x-ray absorption fine-structure measurements at the Co *K*-edge show a local structural anisotropy in fcc $CoPt_3$ nanostructures grown at 300 K on WSe_2. It is characterized by preferential Co-Co bonding along the in-plane direction balanced with preferential heteroatomic bonding along the out-of-plane direction and explains the unexpected perpendicular magnetic anisotropy. Such anisotropy almost vanishes in partially $L1_2$-ordered nanostructures grown at 700 K. In contrast, the short-range order is isotropic in $CoPt_3$ nanostructures grown on NaCl(001) at 370 K. These different behaviors emphasize the favorable role of Se segregated atoms of WSe_2 in the dynamic segregation of Pt atoms at the advancing surface during codeposition, which governs the local structural anisotropy. In the absence of Se, as previously observed in epitaxial $CoPt_3$ films grown on Ru buffer layers, the development of similar structural anisotropy requires higher growth temperatures (550–720 K).

DOI: 10.1103/PhysRevB.81.125417 PACS number(s): 68.35.bd, 75.30.Gw, 75.70.Ak

I. INTRODUCTION

fcc binary alloys M_xPt_{1-x} (M=Cr, Mn, Fe, and Co) prepared in form of thin films may develop peculiar magnetic properties, such as a strong perpendicular magnetic anisotropy (PMA), making them good candidates for ultrahigh-density magnetic recording media. The magnetic response of M_xPt_{1-x} thin films can be strongly modified acting on different parameters: composition, film thickness, deposition temperature, deposition rate, and nature of substrate or by subsequent annealing. It has been demonstrated that the so-called "chemical order," defined by the relative arrangement of M and Pt atoms at long-range as well as short-range scale on the fcc lattice, crucially affects the magnetic properties of these films.[1–6] Molecular-beam epitaxy (MBE) is a powerful method which allows codeposition of metal atoms with an accurate control on several parameters. Owing the very low rate of impinging atoms, MBE deposition allows to finely tune the epitaxial growth and chemical ordering. Furthermore, it has been demonstrated that the growth of continuous films and nanostructures in metastable and frozen-in states may show properties well distinct from those of the equilibrium bulk phases. A remarkable example is given by $CoPt_3$ continuous films which exhibit strong PMA in a certain range of deposition temperatures (T_d=520–750 K, i.e., in the absence of bulk mobility) and independently of the growth direction.[4,7] Such PMA effect, which is expected neither in disordered fcc films nor in $L1_2$-type ordered films, has been demonstrated to mainly originate from an anisotropic chemical short-range order[8] characterized by preferential Co-Co bonds along the in-plane direction and inversely preferential Co-Pt bonds along the out-of-plane direction. In other respects, kinetic Monte Carlo (KMC) simulations of the codeposition process revealed that such anisotropic order could be induced by Co segregation to step edges and Pt segregation to the two low index surfaces.[9] In agreement with theoretical work,[10] x-ray magnetic circular dichroism (XMCD) measurements have demonstrated that the microscopic origin of PMA relies on the anisotropies of Co 3*d*-orbital magnetic moment and Pt 5*d*-orbital moment resulting from the anisotropic 3*d*-5*d* hybridization.[11]

A drastic reduction in the onset temperature of $L1_2$-type long-range order (LRO) was reported for $CoPt_3(111)$ nanostructured films prepared by MBE on $WSe_2(0001)$ substrates.[12] In this system, the weak van der Waals interactions between the metal adatoms and the Se atoms forming the topmost hexagonal plane of the substrate lead to the formation of epitaxially grown nanostructures. These nanostructured films also develop surprisingly strong PMA for deposition temperatures below the onset temperature of ordering ($\sim$400 K) while PMA is vanishing with the appearance of $L1_2$ order. Understanding the relationships between growth conditions, chemical order and magnetic response of these nanostructures is a fundamental issue in sight of potential applications. KMC simulations of the binary-alloy nanostructure growth on weakly interacting substrates, such as WSe_2, were able to qualitatively reproduce the PMA response stemming from a combined effect of Pt surface segregation and flat cluster morphology, the pertinent anisotropy being described by the difference between the numbers of out-of-plane and in-plane Co-Pt bonds in a nanostructure.[13,14] Nevertheless, no experimental verification was achieved.

The main goal of this work is therefore to confirm and quantify such local chemical anisotropy in epitaxial $CoPt_3$ nanostructures on $WSe_2(0001)$. For this purpose, we have

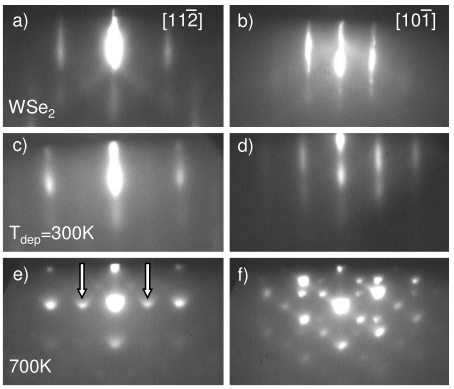

FIG. 1. RHEED patterns along the [11$\bar{2}$] and [10$\bar{1}$] azimuths of the $CoPt_3$ alloy substrate before [(a) and (b)] and after deposition of 3-nm-thick $CoPt_3$ at 300 K [(c) and (d)] and 700 K [(e) and (f)]. The arrows in pattern (e) point out the superlattice spots, signature of $L1_2$ LRO.

used the polarized x-ray absorption fine-structure (XAFS) technique which has demonstrated its ability in providing valuable information on the local chemical order owing to its directional short-range-order sensitivity and its chemical selectivity. Therefore Co *K*-edge polarized XAFS measurements were performed in $CoPt_3(111)$ nanostructures grown at 300 and 700 K.

In order to separate the effect of the reduced size of nanostructures from the role of the substrate on the origin of chemical anisotropy, XAFS experiments were also performed for 001-oriented $CoPt_3$ nanostructures grown on the low-energy surface of NaCl(001) exhibiting no $L1_2$-type LRO up to T_d=670 K. Comparing the short-range ordering found in these two series of nanostructures has allowed us to highlight the role of Se atoms detached from WSe_2 substrate in the atomic exchange processes occurring at the growing facets.

II. SAMPLE PREPARATION, EXPERIMENTAL, AND DATA ANALYSIS

$CoPt_3$ nanostructures were prepared by codeposition of Co and Pt atoms under UHV conditions on freshly cleaved $WSe_2(0001)$ and NaCl(001) substrates. The pressure during deposition did not exceed 5×10^{-9} mbar. Before deposition, the substrates were outgased at 600 K for 1 h. The fluxes of impinging atoms emitted from two e-gun sources were 4.6×10^{-3} Å/s for Co and 2×10^{-2} Å/s for Pt. Depositions were done at 300 and 700 K on $WSe_2(0001)$, and at 370 and 670 K on NaCl(001) surfaces. The nominal thicknesses of the studied samples were equal to 3 nm.

The epitaxial growth was probed *in situ* by reflection high-energy electron diffraction (RHEED). Figure 1 shows RHEED patterns taken along the two main azimuths [11$\bar{2}$] and [10$\bar{1}$] of the $CoPt_3$ alloy before and after deposition of $CoPt_3$ at 300 and 700 K. As previously observed,[15] codeposition of 3-nm-thick $CoPt_3$ on $WSe_2(0001)$ leads to the formation of 111-oriented epitaxial nanostructures with fcc structure even at 300 K. Along the two azimuths, the superlattice spots appearing for T_d=700 K (Fig. 1) confirm the formation of $L1_2$-type LRO.

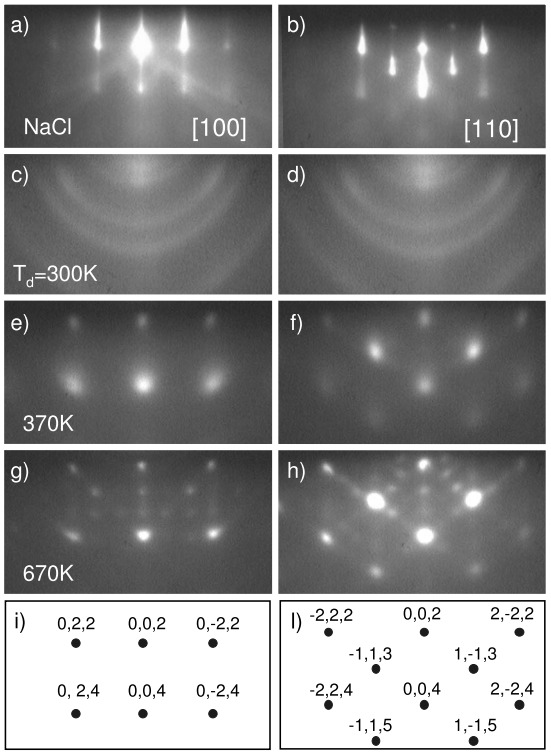

FIG. 2. RHEED patterns taken along the [100] and [110] azimuths of the NaCl(001) substrate before deposition [(a) and (b)] and after 3-nm-thick $CoPt_3$ codeposition at 300 [(c) and (d)], 370 [(e) and (f)], and 670 K [(g) and (h)]. The *hkl* indices of spots refer to a fcc phase with the [001] axis oriented along the surface normal [(i) and (j)].

Deposition of $CoPt_3$ on NaCl(001) leads to the formation of epitaxial 001-oriented fcc nanostructures following a cube-over-cube growth in a temperature range of 370–670 K, as shown by the RHEED patterns (Fig. 2). Such a growth is described by the following epitaxial relationships: [100]NaCl(001)$\|$[100]$CoPt_3$(001) and [110]NaCl(001)$\|$[110]$CoPt_3$, this is quite surprising since the lattice mismatch between NaCl and $CoPt_3$ is about 30%. The separation distances between the substrate streaks and alloy spots correspond roughly to this mismatch, suggesting the formation of stress-free nanostructures. No superstructure spots coming from $L1_2$ ordering are observed even for the deposit at 670 K. The intermediate spots observed in Figs. 2(g) and 2(h) are produced by diffraction on the edges of the thick NaCl substrate. Let us mention that for a more pertinent comparison with 111-oriented $CoPt_3$ nanostructures on WSe_2, codeposition on the NaCl(111) surface would have been better appropriated. However the NaCl(111) surface is heavily charged and then very unstable.[16]

Superconducting quantum interference device magnetometry measurements with magnetic fields applied normal and parallel to the substrate were performed at 300 K in order to verify the occurrence of PMA. While the $CoPt_3(111)$ film grown on $WSe_2(0001)$ at 300 K reveals a perpendicular easy axis of magnetization with full remanence, the film grown at

700 K shows no PMA as discussed in detail in Refs. 15 and 17. In contrast, $CoPt_3$ alloy films grown at 370 K on NaCl(001) show no remanence which is characteristic for a superparamagnetic behavior of the sample as supported by zero-field-cooling and field-cooling measurements. The increase in the deposition temperature to 670 K results in a small opening of the hysteresis loops when measured at 300 K. However, the peculiar shape of the hysteresis loops measured normal and parallel to the substrate plane indicates that a mixture of superparamagnetic and ferromagnetic phases coexist in the sample and show an isotropic behavior which is rather independent of the orientation of the applied field in agreement with the absence of anisotropic short-range order as discussed below. The magnetic properties of the deposits on NaCl(001) are discussed in more detail in the supplementary material to the manuscript.[18]

Two series of polarized x-ray absorption spectroscopy (XAS) experiments at the Co *K*-edge were performed on the CRG-BM08 (Ref. 19) (GILDA) and CRG-BM30 (Ref. 20) (FAME) beamlines at the European Synchrotron Radiation Facilities (ESRF, Grenoble). The $CoPt_3(111)$ samples grown on $WSe_2(0001)$ at 300 and 700 K were measured on the GILDA beamline in fluorescence geometry using a 13 elements Ge multidetector. X-ray absorption data were collected at low temperature ($\sim$10 K) in order to reduce the thermal contribution to structural disorder. Measurements were performed with x-ray polarization vector $\hat{\epsilon}$, oriented nearly parallel ($\theta_{\parallel} \sim 10°$ being the angle between $\hat{\epsilon}$ and the film plane) and nearly perpendicular ($\theta_{\perp} \sim 80°$) to the substrate plane. In order to remove the Bragg peaks of the substrate, several spectra have been collected tilting the sample between $\theta \pm 2.5$ degrees. This movement causes a shift of the substrate peaks on the XAS spectra which are thus well identified and easily removed by interpolation. The $CoPt_3(001)/NaCl(001)$ samples deposited at 370 and 670 K were measured in a similar way on the FAME beamline in fluorescence mode using a 30 elements Ge multidetector. Measurements were performed at $\sim$10 K with the x-ray polarization vector parallel ($\theta_{\parallel}=0°$) and nearly perpendicular ($\theta_{\perp}=80°$) to the substrate plane. For each polarization, the sample orientation was kept fixed. Owing to the large number of detectors covering a wide area, substrate peaks were collected only by a few detectors and easily removed before averaging.

The XAS spectra $\mu_{exp}(E)$, were processed by the ESTRA program[21] which uses the standard method[22] to extract the XAFS structural signal $\chi(k)$. The pre-edge background was fitted by a straight line and subtracted and the postedge atomic background, $\mu_o(E)$, was fitted with a smooth polynomial spline through the data. The XAFS signal was calculated as $\chi(k)=[\mu_{exp}(k)-\mu_o(k)]/\mu_o(k)$. The energy scale for the photoelectron wave vector ($k=\hbar^{-1}\sqrt{2m(E-E_0)}$) was defined choosing the edge energy (E_0) at the first maximum of $\mu_{exp}(E)$ first derivative (the energy shift among the data was less than ± 0.5 eV), then the energy shift, ΔE_0, was kept fixed during the refinement for all the spectra. The analysis of the polarized XAFS spectra was performed by fitting the k^2-weighted $\chi(k)$ to the standard XAFS formula,[22] using the FITEXA program,[21] as described in detail in the Appendix.

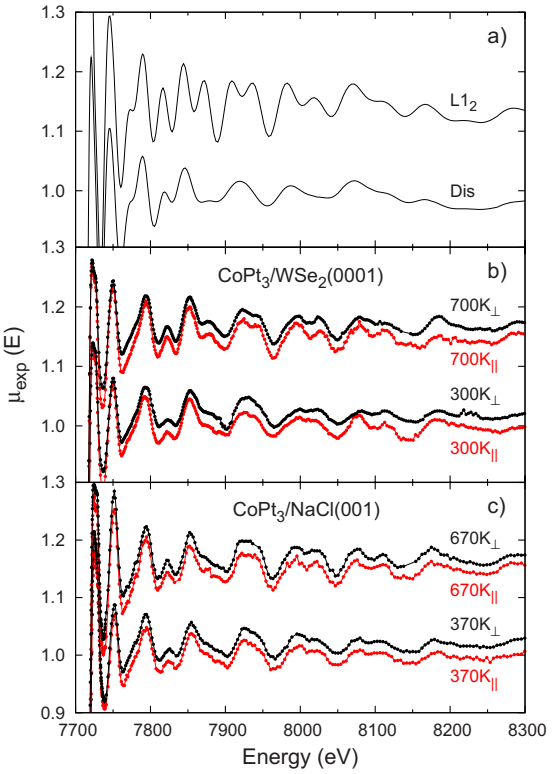

FIG. 3. (Color online) Simulated Co *K*-edge x-ray absorption spectra (XAS) for the $L1_2$ ordered and fcc disordered (Dis) $CoPt_3$ phases (a); normalized experimental spectra measured for $CoPt_3(111)$ grown on $WSe_2(0001)$ at 300 and 700 K (b) and $CoPt_3(001)$ grown on NaCl(001) at 370 and 670 K (c), for in-plane $\parallel$ (red dots) and out-of plane $\perp$ (black dots) geometries (spectra are shifted for clarity).

The experimental spectra of the four studied samples measured for the two polarization geometries are shown in Fig. 3. For comparison, also presented are the spectra calculated for a perfectly $L1_2$-ordered $CoPt_3$ structure and a randomly disordered (Dis) fcc structure. The simulations were performed using the FEFF8.2 code[23] for atomic clusters of 6 Å radii. The Dis spectrum is an average signal obtained by considering different disordered configurations around Co in order to reproduce an homogeneous chemical disorder in the alloy. The simulations demonstrate that the signals of the $L1_2$ and fcc disordered structures are independent of the polarization direction. Therefore, any polarization dependence observed on the experimental data must be the fingerprint of structural and/or chemical anisotropy.

The spectra of the $CoPt_3(111)/WSe_2(0001)$ samples present clear differences as a function of the growth temperature and a pronounced polarization dependence for the sample grown at 300 K. These features are also visible in the moduli of the Fourier transforms (FTs) of the k^2-weighted XAFS signal shown in Fig. 4. For the sample grown at 300 K, the peaks are broader and weaker, close to those of the Dis signal and the polarization effect is accentuated between 3 and 4.5 Å. In contrast, the signals of the $CoPt_3/NaCl$ samples present no clear polarization effect. An increase in the intensities of the peaks around 2.5 and 5 Å with the growth temperature is characteristic for an enhancement of the $L1_2$ ordering.

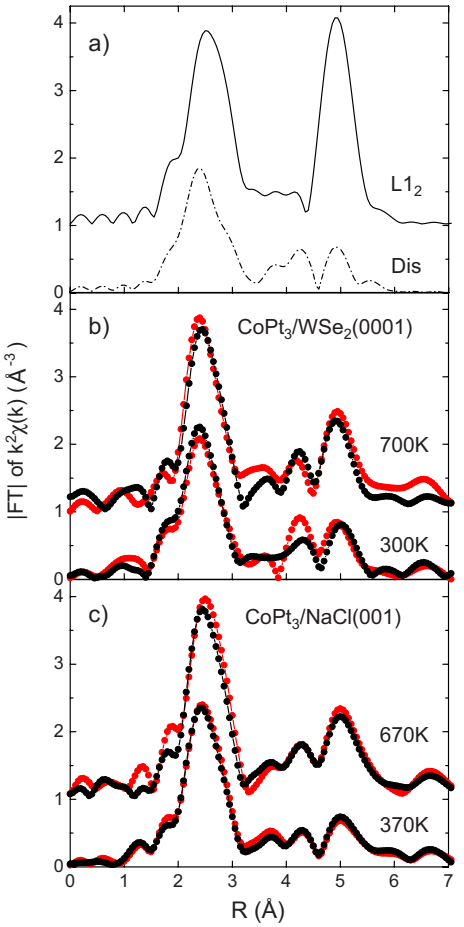

FIG. 4. (Color online) Moduli of the Fourier transforms of the k^2-weighted $\chi(k)$ signals of the reference structures ($L1_2$ and Dis) and the four samples, for in-plane (red dots) and out-of-plane (black dots) polarization geometries (k range: 4–12 Å).

Thus, the FTs offer an intuitive interpretation of the local structure around the Co atoms, keeping in mind that the photoelectron phase-shift effect gives rise to an apparent contraction of interatomic distances around 0.3–0.6 Å. The first peak centered around 2.5 Å represents the Co-$(Co/Pt)_1$ nearest-neighbor shell, and is associated with the SS_1 path in Fig. 7. The structural features observed between 3.5 and 6 Å are associated to single- and multiple-scattering paths, namely, the SS_2 and SS_3 single-scattering paths and the MS_4. The latter accounts for single- as well as multiple-scattering contributions from colinear atomic arrangement along the diagonals of the fcc cube faces as described in the Appendix. The XAFS signals for $CoPt_3(111)/WSe_2(0001)$ are well reproduced by considering these four contributions in the standard XAFS formula. For the $CoPt_3(001)/NaCl(001)$ samples, an additional single-scattering contribution coming from the fifth neighbor, noted SS_5, is required to statistically improve the refinement. The neighbor positions around the absorbing Co_0 atom are illustrated by the schematic top views in Fig. 7 of the Appendix. For both polarization geometries, the best fits of the k^2-weighted $\chi(k)$ signals and their corresponding FTs are shown in Fig. 5 for $CoPt_3(111)/WSe_2(0001)$ and in Fig. 6 for $CoPt_3(001)/NaCl(001)$.

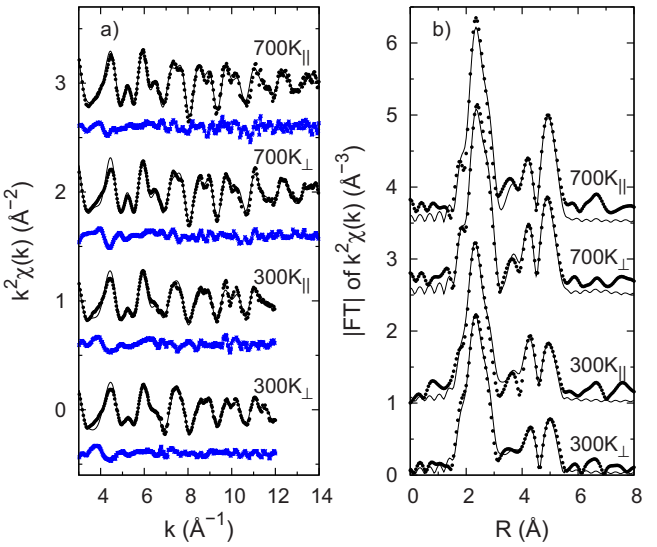

FIG. 5. (Color online) (a) Experimental (dots) and best-fitted (solid lines) $k^2\chi(k)$ curves for $CoPt_3(111)/WSe_2(0001)$ samples grown at 300 and 700 K, for in-plane ($\parallel$) and out-of plane ($\perp$) polarizations measurements. For each fit the residual $k^2\chi(k)_{exp}-k^2\chi(k)_{fit}$ is shown (blue dots). (b) The corresponding FT moduli of the experimental (dots) and best-fitted (solid line) curves (k range: 3–12 Å).

III. RESULTS AND DISCUSSION

The structural parameters extracted from the refinement of the $CoPt_3(111)/WSe_2(0001)$ XAFS spectra are reported in Table I. The analysis of polarized XAFS spectra leads to effective coordination numbers for parallel $\tilde{N}_\parallel$ and perpendicular $\tilde{N}_\perp$ polarization geometries (see Appendix for a de-

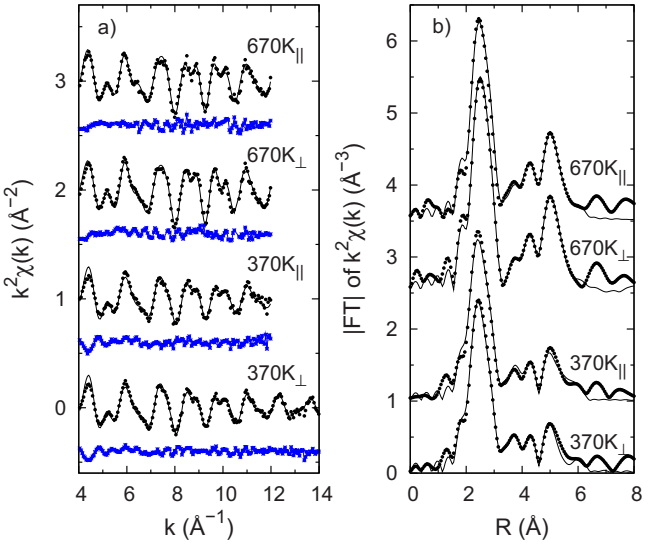

FIG. 6. (Color online) (a) Experimental (dots) and best-fitted (solid lines) $k^2\chi(k)$ curves for $CoPt_3(001)/NaCl(001)$ samples grown at 370 and 670 K, for in-plane ($\parallel$) and out-of plane ($\perp$) polarizations measurements. For each fit the residual $k^2\chi(k)_{exp}-k^2\chi(k)_{fit}$ is shown (blue dots). (b) The corresponding FT moduli of the experimental (dots) and best-fitted (solid line) curves (k range: 4–12 Å).

TABLE I. Structural parameters obtained from the refinement of polarized XAFS data for $CoPt_3(111)/WSe_2(0001)$ samples. For each shell (j) and each type of neighbor, the in-plane N^{in} and the out-of-plane N^{out} coordination numbers (deduced from the adjusted effective numbers) are reported for emphasizing the chemical anisotropy. For the fourth shell, only the sums of the Co_0Pt_1-Co_4 and Co_0-Co_1-Co_4 contributions are given, deduced from the relation given in Ref. 24. R-factor values give a quantitative estimation of the quality of fitting.

Signal	Scatters	$\tilde{N}^j_\perp$	$R^j_\perp$ (Å)	$\tilde{N}^j_\parallel$	$R^j_\parallel$ (Å)	N^{out}	N^{in}
			$CoPt_3/WSe_2(0001)$-T_d=300 K				
SS_1	Pt_1	10.3(3)	2.67(1)	9.3(2)	2.67(1)	5.15	4.48
	Co_1	1.7	2.64(1)	2.7	2.66(1)	0.85	1.52
SS_2	Pt_2	2.6(2)	3.72(2)	2.6	3.72	2.6	
	Co_2	3.4	3.79(2)	3.4	3.79	3.4	
SS_3	Pt_3	17.1(5)	4.70(3)	15.2(5)	4.65(3)	12.8	3.0
	Co_3	6.9	4.84(3)	8.8(1)	4.73(3)	5.2	3.0
MS_4-I	Co_4	9.1	5.32(3)	7.9	5.32(3)	4.55	3.75
R^2		0.06		0.07			
			$CoPt_3/WSe_2(0001)$-T_d=700 K				
SS_1	Pt_1	10.2(4)	2.68(1)	10.0(3)	2.68(1)	5.10	5.00
	Co_1	1.8	2.68(1)	2.0	2.66(1)	0.90	1.00
SS_2	Pt_2	0.1		0.00		0.1	
	Co_2	5.9(1)	3.75(2)	5.9	3.75	5.9	
SS_3	Pt_3	19.9(8)	4.67(3)	20.9(6)	4.70(3)	14.9	5.6
	Co_3	4.1	4.69(3)	3.1	4.90(3)	3.1	0.4
MS_4-I	Co_4	9.0	5.30(3)	8.61	5.28(3)	4.5	4.24
R^2		0.07		0.06			

tailed description). In each shell, the total effective coordination numbers are constrained to the crystallographic values (N_{tot}) recalled in Table III for the $L1_2$-ordered $CoPt_3$ structure. Therefore, as shown in Table I, for each shell $N^j_{tot}=\tilde{N}^j_\perp=\tilde{N}^j_\parallel$ with $\tilde{N}^j_{\perp(\parallel)}=\tilde{N}^j_{\perp(\parallel),Pt}+\tilde{N}^j_{\perp(\parallel),Co}$.

For the sample grown at 300 K, the Co-Co_1 effective correlations correspond to 23% of the in-plane contributions, i.e., the percentage for a disordered alloy, and 14% of the out-of-plane contributions. This difference is even stronger in the third coordination shell and thus reveals an in-plane Co segregation. For the sample grown at 700 K, this tendency is vanishing in the first shell and twice smaller in the third shell. On the contrary, the high occupancy rates of Pt in the first and third shells as well as the one of Co atoms in the second shell, almost independent of polarization, are characteristic for a high degree of chemical order in agreement with the isotropic $L1_2$ long-range order, observed by RHEED. After numerous simulations, it turns out that the contribution of the fourth shell is dominated by the almost collinear Co-Pt-Co configurations. The effective coordination numbers for the fourth shell is reported in Table I just for the single scattering and without error since they are related to the probabilities to find Co-Pt and Co-Co nearest-neighbor pairs associated with the first shell.

For the sample grown at 300 K, the first-nearest Co-Co_1 distances are slightly shorter than the Co-Pt_1 ones while the inverse is obtained for the second and third shells. For the sample grown at 700 K, these differences have almost disappeared as expected for the Co-Co_3 distance from parallel polarization data. However, since the $R_\parallel$ distances are intermediate values between real in-plane and out-of-plane distances, they are difficult to be interpreted. Nevertheless, deviations from the ratio between the first and third distances equal to $\sqrt{3}$ in a perfect fcc lattice are significant only for the Co-Co pairs and can be related to the in-plane Co segregation.

The local chemical anisotropy observed only in the sample grown at 300 K can be associated with the anisotropic Co segregation forming small (nanometric and subnanometric sizes) Co-rich regions in form of platelets. Such anisotropic chemical distribution was already observed in $CoPt_3$ continuous films[8] but grown at higher temperature (690 K) and was proven to be the origin of the perpendicular magnetic anisotropy. As a matter of fact, such anisotropic $3d$-$5d$ hybridization and the strong spin-orbit coupling of Pt atoms lead to an anisotropy of the $3d$-orbital magnetic moment and an angular dependence of the Pt orbital moment as evidenced from angular-dependent XMCD measurements.[11]

For $CoPt_3/WSe_2$, two explanations can be put forward for the appearance of the structural anisotropy already at 300 K. The first one could be related to the nanostructured morphology of the $CoPt_3$ alloy as observed by scanning tunneling microscopy[25] and characterized by an average lateral grain size of 4 nm. This morphology would favor atomic exchange between Co and Pt atoms not only on the top facet but also on the side-walled facets. However, the relatively low growth temperature is not favorable for the Co segregation at

TABLE II. Structural parameters obtained from the refinement of polarized XAFS data for $CoPt_3(001)/NaCl(001)$ samples. For the first four shells, the definitions of parameters are identical with those in Table I. For the fifth shell only single scattering is taken into account.

Signal	Scatters	$\tilde{N}^j_\perp$	$R^j_\perp$ (Å)	$\tilde{N}^j_\parallel$	$R^j_\parallel$ (Å)	N^{out}	N^{in}
			$CoPt_3/NaCl(001)$-T_d=370 K				
SS_1	Pt_1	10.8(4)	2.68(1)	10.8(2)	2.69(1)	7.20	3.60
	Co_1	1.2	2.66(1)	1.2	2.66(1)	0.80	0.40
SS_2	Pt_2	0.9	3.65(1)	1.0	3.60(2)	0.31	0.64
	Co_2	5.1(2)	3.79(1)	5.0(2)	3.79(2)	1.69	3.36
SS_3	Pt_3	20.1(5)	4.71(2)	20.1	4.71	20.1	
	Co_3	3.9	4.47(2)	3.9	4.47	3.9	
MS_4-I	Co_4	9.8	5.36(5)	9.8	1.17(4)	7.20	3.59
SS_5	Pt_5	12.0(5)	6.09(2)	12.0(2)	6.10(2)	8.00	4.01
	Co_5	12.0	5.93(2)	12.0	5.94(2)	8.00	3.99
R^2			0.07		0.08		
			$CoPt_3/NaCl(001)$-T_d=670 K				
SS_1	Pt_1	11.9(1)	2.70(1)	11.4(4)	2.70(1)	7.86	3.67
	Co_1	0.1	2.75(1)	0.6	2.69(1)	0.04	0.33
SS_2	Pt_2	0.2	3.65(2)	0.2	3.80(2)	0.00	0.1
	Co_2	5.8(2)	3.79(2)	5.8(2)	3.79(2)	2.00	3.9
SS_3	Pt_3	23.3(5)	4.72(2)	23.3	4.72	23.3	
	Co_3	0.7	4.55(2)	0.7	4.55	0.7	
MS_4-I	Co_4	11.8	5.40(2)	10.9	0.16	8.00	4.00
SS_5	Pt_5	14.8(5)	6.01(2)	16.2(5)	6.02(2)	9.86	5.87
	Co_5	9.2	6.02(2)	7.8	6.04(2)	6.14	2.13
R^2			0.05		0.06		

step edges which was found to be the preliminary process before the formation of Co platelets resulting from the coalescence of islands.[9] The second explanation would come from a conjugated effect between Pt surface segregation which was assumed to be the origin of PMA in continuous $CoPt_3$ films[13,14,26] along the Se surface segregation. The latter one was clearly identified by Auger electron spectroscopy on the top layer of a 3-nm-thick FePt alloy grown at room temperature on WSe_2.[27] For higher deposition temperatures, the surface segregation of Se leads even to the formation of a Moiré pattern after the deposition of 7-nm-thick Pt at 770 K.[28]

To disentangle these two possible explanations, the idea was to perform a similar XAFS analysis in $CoPt_3$ nanostructures grown on NaCl(001). The experimental k^2-weighted $\chi(k)$ are well represented by the contributions of neighbors located in the first five shells and the agreement in the moduli of the FTs is perfect up to 6 Å (Fig. 3). The structural parameters obtained from the simulations are summarized in Table II.

The coordination numbers as well as the interatomic distances reflect no polarization dependence, indicating an overall isotropic local order for the sample deposited at 370 K on the NaCl substrate. For both samples, the numbers of Pt neighbors in the first and third shell are much larger than those corresponding to a randomly disordered structure, the same feature for the Co neighbors in the second and fourth shells. For the sample grown at 670 K, the coordination numbers (excepted for the fifth shell rather Co enriched) are very close to those found in a perfectly ordered structure which is listed in Table III. Let us note that for this sample, there are more out-of-plane Co_0-Pt_1 pairs than in-plane Co_0-Pt_1 pairs, and this result would be consistent with the relaxation behavior toward the $L1_2$ structure observed in $Cu_3Au(001)$ oriented crystal where the relaxation time was found 20 times faster along the normal to the surface than in the plane.[29]

Finally, for the two $CoPt_3/NaCl$ samples, the XAFS analysis shows an overall isotropic local order with no in-plane Co segregation in the first four shells. From these results we can exclude an effect of reduced size as the origin of the Co platelets in the sample grown at 300 K on WSe_2 since the nanostructures grown on NaCl have similar sizes.[25] The higher growth temperature (370 K) necessary to form epitaxial nanostructures on NaCl is still in the temperature range for which PMA is observed in $CoPt_3/WSe_2$ nanostructures.[15] Thus, a growth temperature effect can also be excluded. Moreover, an effect of the growth direction on the formation of Co platelets could be possible. However, this statement can also be disproved. As a matter of fact, on the one hand, the deposition temperature range for which PMA is observed in disordered fcc $CoPt_3$ continuous films was demonstrated

TABLE III. Type and number of neighbors in the Single-scattering and multiple-scattering processes for the $L1_2$-ordered $CoPt_3$ phase. The distances, R_j are indicated as a function of the lattice parameter of the fcc lattice, a. The MS_4 signal is composed of single-(I), double-(II), and triple-(III) scattering processes. N_{tot} is the total number of paths per absorbing atoms. N^{in} is the number of independent paths per absorbing atoms occurring strictly in the grown [(111) or (001)] plane while N^{out} is the number of paths out of the grown plane. $\tilde{N}_{\perp}^{in}(_{\parallel})$ is the effective number of in-plane contributions observed in perpendicular (parallel) polarization geometry, and $\tilde{N}_{\perp}^{out}(_{\parallel})$ is the effective number of out-of plane contributions observed in perpendicular (parallel) polarization geometry.

				(111) plane						(001) plane					
Signal	R_j	N_{tot}	Scatterer(s)	N^{out}	N^{in}	$\tilde{N}_{\perp}^{out}$	$\tilde{N}_{\perp}^{in}$	$\tilde{N}_{\parallel}^{out}$	$\tilde{N}_{\parallel}^{in}$	N^{out}	N^{in}	$\tilde{N}_{\perp}^{out}$	$\tilde{N}_{\perp}^{in}$	$\tilde{N}_{\parallel}^{out}$	$\tilde{N}_{\parallel}^{in}$
SS_1	$a/\sqrt{2}$	12	Pt_1	6	6	12	0	3	9	8	4	12	0	6	6
SS_2	a	6	Co_2	6		6	0	6	0	2	4	6	0	0	6
SS_3	$a\sqrt{3/2}$	24	Pt_3	18	6	24	0	15	9	24		24	0	24	6
MS_4	$a\sqrt{2}$ I	12	Co_4	6	6	12	0	3	9	8	4	12	0	6	6
	II	24	Co_4-Pt_1	12	12	24	0	6	18	16	8	24	0	12	12
	III	12	Pt_1-Co_4-Pt_1	6	6	12	0	3	9	8	4	12	0	6	6
SS_5	$a\sqrt{5/2}$	24	Pt_3	24		24	0	24	0	16	8	24	0	12	12

to be largely independent on the growth direction.[7] On another hand, Pt was shown to segregate indifferently to the surfaces of a (111) (Ref. 30) or (001) (Ref. 31) Co-Pt alloy. For these reasons only segregation of Se atoms detached from the WSe_2 surface can explain our experimental results. It is noticeable here that taking into account Co-Se correlations does not improve significantly the refinement of the data in spite of an increase in adjusted parameters. This suggests that Se atoms segregate continuously at the growing surface during codeposition so that they are finally located in the topmost layer of the nanostructures. Therefore the fraction of Co-Se correlations is to low to be visible in our XAFS spectra. Such segregated Se atoms would behave as vacancies favoring the atomic exchanges between Co and Pt atoms which are driven by the tendency of Pt atoms to segregate to the advancing surface. These processes would lead to the formation of Co platelets which are covered by the successive layers and frozen in at 300 K due to negligible bulk mobility. By increasing the growth temperature and relying on a similar mechanism, Se atoms would then favor the $L1_2$ order which is already observed in nanostructures prepared at growth temperatures as low as 420 K.

IV. SUMMARY

Polarized XAFS measurements at the Co K-edge were performed in two series of epitaxial $CoPt_3$ nanostructures grown on WSe_2(0001) and NaCl(001) surfaces. A detailed analysis of the XAFS data reveals an anisotropic chemical order around Co absorbing atoms extended up to the fourth neighbors only in the $CoPt_3/WSe_2$ sample grown at 300 K. This structural anisotropy is characterized by preferential in-plane Co-Co bonds which suggests the existence of Co-rich regions in form of thin disks, with nanometric diameter, parallel to the film plane. These disks are the source of the PMA measured in this sample. For the $CoPt_3/WSe_2$ sample grown at 700 K, the structural anisotropy vanishes almost completely in agreement with the observed $L1_2$ ordering which due to its isotropic character suppresses PMA. The absence of a structural anisotropy in the two $CoPt_3/NaCl$ samples grown at 370 and 670 K highlights the role of segregated Se atoms during codeposition. Conjugated with the well-established Pt surface segregation, the Se segregation seems to be the mechanism favoring the development of a local structural anisotropy in $CoPt_3$ nanostructures grown on WSe_2 at a temperature as low as 300 K. Furthermore, the same Se atoms behaving as vacancies during the codeposition would also favor the $L1_2$ ordering at growth temperature above 420 K.

ACKNOWLEDGMENTS

Allocation of beamtime on the Italian CRG-BM08 and French CRG-BM30 beamlines at the ESRF is gratefully acknowledged. The authors thank J. L. Hazemann (BM30) and F. Bardelli (BM08) for their helpful support on running the beamlines. This work was supported in part by the Deutscher Akademischer Austauschdienst and French partenariat Hubert Curien (Procope).

APPENDIX: POLARIZED XAFS DATA ANALYSIS

The quantitative refinement of the polarized XAFS spectra recorded at the Co K-edge allow the determination of the relevant structural parameters which describe in detail the local order around the Co absorbing atoms. They were derived by fitting the experimental spectra to the theoretical XAFS formula,[22]

$$k\chi_{th}(k) = S_0^2 \sum_j \frac{\tilde{N}_j}{R_j^2} F_j e^{-2k^2\sigma_j^2} e^{-2R_j/\lambda} \sin(2kR_j + \phi_j), \quad \text{(A1)}$$

where R_j is the mean distance between the absorbing atom and the neighbors in the jth shell and σ_j^2 the mean-square relative displacement (Debye-Waller factor). $F_j(k)$, $\phi_j(k)$, and $\lambda(k)$ are, respectively, the backscattering amplitude, the total phase shift and the mean-free path of photoelectron; they are calculated by the FEFF code[23] using, as models,

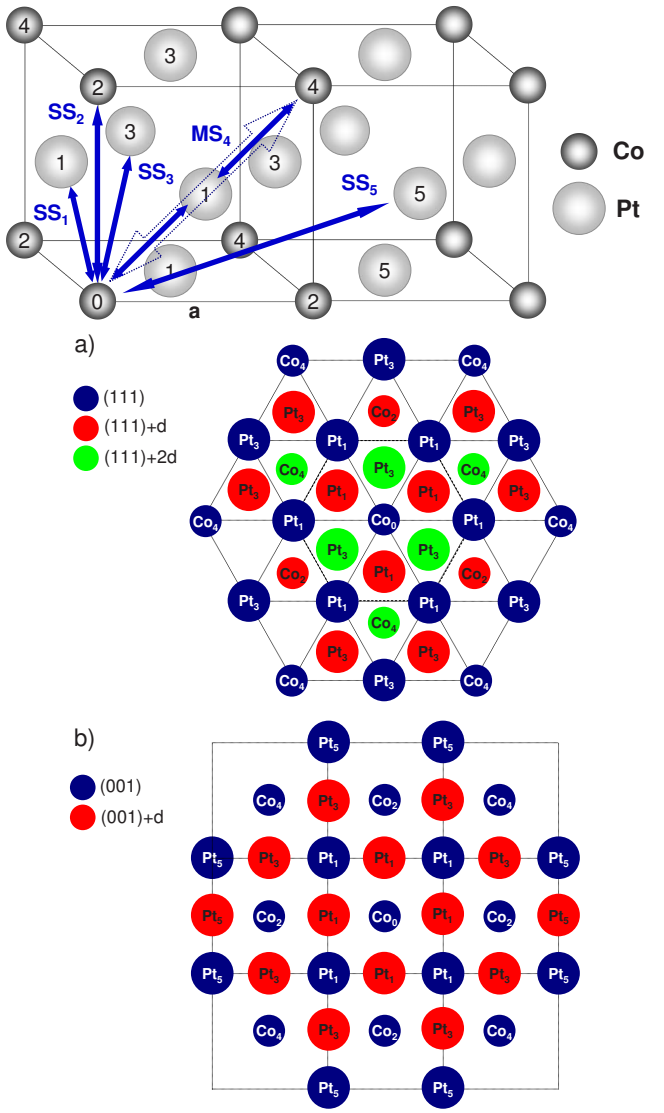

FIG. 7. (Color online) Top: view of the $L1_2$-ordered structure and the scattering paths used in the fitting. Bottom: schematic top view of $L1_2$ structure for (a) $CoPt_3(111)/WSe_2(0001)$ and (b) $CoPt_3(001)/NaCl(001)$. In blue, the neighbors in the sample plane as the absorbing atom, in red and green, the atoms located in the first and second upper planes.

$CoPt_3$ clusters with fully ordered $L1_2$ phase (shown in Fig. 7) and randomly disordered fcc solid solution as already done for $CrPt_3$ continuous films.[32] S_0^2 is an empirical parameter taking into account losses due to many-body effects, and kept fixed for all spectra; an optimized value of 0.75 was thus chosen. The effective coordination numbers, $\tilde{N}_j$, take into account the polarization dependence of the photoabsorption process and are given by[22]

$$\tilde{N}_j = 3\sum_{i=1}^{N_j} \cos^2 \alpha_{ji}, \tag{A2}$$

where α_{ij} is the angle between the x-ray polarization vector ($\hat{\epsilon}$) and the bond direction between the absorbing atom and the ith scatterer in the jth coordination shell. These numbers can be expressed as a function of the true in-plane, N^{in}, and out-of-plane, N^{out}, neighbors, i.e., (i) atoms in the same plane as the absorbing atom, namely (111) and (001) planes for $CoPt_3$ nanostructures grown on $WSe_2(0001)$ and NaCl(001), respectively, and (ii) atoms out of these planes.

In a fcc lattice, their expressions for the two polarization geometries ($\tilde{N}_\perp$ and $\tilde{N}_\parallel$) are deduced from Eq. (A2). For a (111) growth plane, they are calculated for each shell as follows:

Shell	$\tilde{N}_\perp$	$\tilde{N}_\parallel$
S_{I}	$2N^{out}$	$1.5N^{in}+0.5N^{out}$
S_{II}	N^{out}	N^{out}
S_{III}	$\frac{4}{3}N^{out}$	$1.5N^{in}+0.83N^{out}$
S_{IV}	$2N^{out}$	$1.5N^{in}+0.5N^{out}$

and for a (001) growth plane,

Shell	$\tilde{N}_\perp$	$\tilde{N}_\parallel$
S_{I}	$1.5N^{out}$	$1.5N^{in}+0.75N^{out}$
S_{II}	$3N^{out}$	$1.5N^{in}$
S_{III}	N^{out}	N^{out}
S_{IV}	$1.5N^{out}$	$1.5N^{in}+0.75N^{out}$
S_{V}	$1.5N^{out}$	$1.5N^{in}+0.75N^{out}$

It is worth noting that for both planes, the measurements with perpendicular polarization probe only the contributions of out-of-plane neighbors while the measurements with parallel polarization probe the contributions of in-plane and out-of-plane neighbors. Table III shows for both polarization geometries the effective and true numbers calculated for a perfectly ordered $L1_2$-type structure with respect to the two growth planes. Independently of polarization and for any shell, $\tilde{N}^{in}_{\parallel(\perp)}+\tilde{N}^{out}_{\parallel(\perp)}$ is always equal to the total number of neighbors $N_{tot}=N^{in}+N^{out}$. It demonstrates that the XAFS signals of a perfectly ordered $L1_2$-type phase or a randomly disordered fcc phase are independent of polarization. Therefore, any differences in the XAFS spectra with polarization are associated to an anisotropy in the sites of Co and Pt neighbors with respect to the growth plane.

The refinements of the experimental spectra were performed through a least-squares minimization procedure, by fitting the k^2-weighted $\chi(k)$ signal without Fourier filtering. They were performed adding successively new contributions and checking their effective statistical significance. Finally, reduced sets of neighbor shells, four shells for $CoPt_3/WSe_2$ (Table I) and five shells for $CoPt_3/NaCl$ (Table II) were considered. Constraints between parameters were applied, based on the crystallographic structure and chemical composition. For example, the total effective coordination numbers in each shell were fixed to the values calculated in Table III. Only the atomic fractions of Co and Pt were refined and therefore the alloy composition can vary from one shell to another one. In each shell, the Debye-Waller factors were assumed to be identical for Co and Pt atoms. This choice was mandatory, otherwise the well-known strong correlation between N and σ would give less reliable results.

The refinement of the fourth shell does require great care. Its important contribution originates from the atomic alignments along the diagonals of the cube face (Fig. 7). Owing to the collinear atomic configurations Co_0-X_1-Y_4, the multiple-scattering terms, namely, the double-scattering (Co_0-X_1-Y_4-Co_0 and Co_0-Y_4-X_1-Co_0) and the triple-scattering (Co_0-X_1-Y_4-X_1-Co_0) paths, are important and have to be considered in addition to the single-scattering path, Co_0-Y_4. For a disordered configuration the X and Y can be Co or Pt, therefore four configurations must be considered. After several attempts, we found that the MS_4 contributions are largely dominated by Co-Pt_1-Co_4 configurations while the Co-Co_1-Co_4 configurations are definitively weaker. The probabilities of the different contributions were derived from those of the Co-Pt and Co-Co nearest-neighbor pairs deduced from the coordination numbers in order to reduce the number of parameters and the correlations among them.[24]

The path lengths of MS_4 contributions were calculated using the nearest-neighbor distances, the bond angles were found close to 180° within the experimental uncertainty. The in-plane distances and neighbors were obtained from the simulations of the spectra measured with parallel polarization, by fixing the parameters corresponding to out-of-plane neighbors to those deduced from the simulations of the spectra measured with perpendicular polarization.

[1] D. Weller, H. Brändle, G. L. Gorman, C. J. Lin, and H. Notarys, Appl. Phys. Lett. **61**, 2726 (1992).

[2] P. W. Rooney, A. L. Shapiro, M. Q. Tran, and F. Hellman, Phys. Rev. Lett. **75**, 1843 (1995).

[3] R. F. C. Farrow, D. Weller, R. F. Marks, M. F. Toney, A. Cebollada, and G. R. Harpd, J. Appl. Phys. **79**, 5967 (1996).

[4] M. Maret, M. Cadeville, R. Poinsot, A. Herr, E. Beaurepaire, and C. Monier, J. Magn. Magn. Mater. **166**, 45 (1997).

[5] M. Maret, M. C. Cadeville, A. Herr, R. Poinsot, E. Beaurepaire, S. Lefebvre, and M. Bessière, J. Magn. Magn. Mater. **191**, 61 (1999).

[6] M. Maret, M. Albrecht, J. Köhler, R. Poinsot, C. Ulhaq-Bouillet, J. Tonnerre, J. Berar, and E. Bucher, J. Magn. Magn. Mater. **218**, 151 (2000).

[7] A. L. Shapiro, P. W. Rooney, M. Q. Tran, F. Hellman, K. M. Ring, K. L. Kavanagh, B. Rellinghaus, and D. Weller, Phys. Rev. B **60**, 12826 (1999).

[8] C. Meneghini, M. Maret, V. Parasote, M. Cadeville, J. Hazemann, R. Cortes, and S. Colonna, Eur. Phys. J. B **7**, 347 (1999).

[9] B. B. Maranville, M. Schuerman, and F. Hellman, Phys. Rev. B **73**, 104435 (2006).

[10] P. Bruno, Phys. Rev. B **39**, 865 (1989).

[11] W. Grange, M. Maret, J. P. Kappler, J. Vogel, A. Fontaine, F. Petroff, G. Krill, A. Rogalev, J. Goulon, M. Finazzi, and N. B. Brookes, Phys. Rev. B **58**, 6298 (1998).

[12] M. Albrecht, A. Maier, F. Treubel, M. Maret, R. Poinsot, and G. Schatz, Europhys. Lett. **56**, 884 (2001).

[13] S. Heinrichs, W. Dieterich, and P. Maass, Europhys. Lett. **75**, 167 (2006).

[14] S. Heinrichs, W. Dieterich, and P. Maass, Phys. Rev. B **75**, 085437 (2007).

[15] A. Maier, B. Riedlinger, F. Treubel, M. Maret, M. Albrecht, E. Beaurepaire, J. M. Tonnerre, and G. Schatz, J. Magn. Magn. Mater. **240**, 377 (2002).

[16] W. Hebenstreit, M. Schmid, J. Redinger, R. Podloucky, and P. Varga, Phys. Rev. Lett. **85**, 5376 (2000).

[17] M. Albrecht, M. Maret, A. Maier, F. Treubel, B. Riedlinger, U. Mazur, G. Schatz, and S. Anders, J. Appl. Phys. **91**, 8153 (2002).

[18] See supplementary material at http://link.aps.org/supplemental/10.1103/PhysRevB.81.125417 for the magnetic properties of $CoPt_3$ films grown on NaCl(001).

[19] S. Pascarelli, F. Boscherini, F. D'Acapito, J. Hrdy, C. Meneghini, and S. Mobilio, J. Synchrotron Radiat. **3**, 147 (1996).

[20] O. Proux, X. Biquard, E. Lahera, J. J. Menthonnex, A. Prat, O. Ulrich, Y. Soldo, P. Trvisson, G. Kapoujyan, G. Perroux, P. Taunier, D. Grand, P. Jeantet, M. Deleglise, J. P. Roux, and J. L. Hazemann, Phys. Scr. **T115**, 970 (2005).

[21] C. Monesi, C. Meneghini, F. Bardelli, M. Benfatto, S. Mobilio, U. Manju, and D. D. Sarma, Phys. Rev. B **72**, 174104 (2005). ESTRA and FITEXA programs are available online at: http://webusers.fis.uniroma3.it/~meneghini/software.html

[22] P. A. Lee, P. H. Citrin, P. Eisenberger, and B. M. Kinkaid, Rev. Mod. Phys. **53**, 769 (1981).

[23] S. I. Zabinsky, J. J. Rehr, A. Ankudinov, R. C. Albers, and M. J. Eller, Phys. Rev. B **52**, 2995 (1995).

[24] If $P(Co_0\text{-}Pt_1)=x$ is the probability to find a Co-Pt nearest-neighbor pair, the following probabilities can be calculated for the other configurations: $P(Co_0\text{-}Co_1)=1-x$; $P(Co_0\text{-}Pt_1\text{-}Co_4)=x^2$; $P(Co_0\text{-}Co_1\text{-}Co_4)=(1-x)^2$; $P(Co_0\text{-}Co_1\text{-}Pt_4)=(1-x)x=x-x^2$; $P(Co_0\text{-}Pt_1\text{-}Pt_4)=(1-x)x=x-x^2$; $P(Co_0\text{-}Co_4)=P(Co_0\text{-}Pt_1\text{-}Co_4)+P(Co_0\text{-}Co_1\text{-}Co_4)=2x^2-2x+1$; and $P(Co_0\text{-}Pt_4)=P(Co_0\text{-}Co_1\text{-}Pt_4)+P(Co_0\text{-}Pt_1\text{-}Pt_4)=2x-2x^2$.

[25] F. Liscio, Ph.D. thesis, Institut Polytechnique Grenoble and Roma Tre University, 2009.

[26] V. Pierron-Bohnes, M. Maret, L. Bouzidi, and M. Cadeville, *N057, Diffusion Mechanisms in Crystalline Materials*, MRS Symposium Proceedings No. 57 (Materials Research Society, Pittsburgh, 1998).

[27] M. Maret, B. Gilles, I. L. Guhr, B. Riedlinger, M. Albrecht, G. Schatz, and E. Beaurepaire, Nanotechnology **15**, 1590 (2004).

[28] D. Makarov, R. Pallesche, M. Maret, T. Ulbrich, G. Schatz, and M. Albrecht, Surf. Sci. **601**, 2032 (2007).

[29] H. Reichert, P. J. Eng, H. Dosch, and I. K. Robinson, Phys. Rev. Lett. **78**, 3475 (1997).

[30] Y. Gauthier, R. Baudoing-Savois, J. Bugnard, U. Bardi, and A. Atrei, Surf. Sci. **276**, 1 (1992).

[31] U. Bardi, A. Atrei, P. Ross, E. Zanazzi, and G. Rovida, Surf. Sci. **211-212**, 441 (1989).

[32] M. Maret, F. Bley, C. Meneghini, M. Albrecht, J. Köhler, E. Bucher, and J. Hazemann, J. Phys.: Condens. Matter **17**, 2529 (2005).